Characteristics that Produce White-light Enhancements in Solar Flares Observed by *Hinode*/SOT

Kyoko Watanabe[1], Jun Kitagawa[2], and Satoshi Masuda[2]

[1] National Defense Academy of Japan, 1-10-20 Hashirimizu, Yokosuka 239-8686, Japan; kwatana@nda.ac.jp
[2] Institute for Space-Earth Environmental Research (ISEE), Nagoya University, Furo-cho, Chikusa-ku, Nagoya 464-8601, Japan

Abstract

To understand the conditions that produce white-light (WL) enhancements in solar flares, a statistical analysis of visible continuum data as observed by *Hinode*/Solar Optical Telescope (SOT) was performed. In this study, approximately 100 flare events from M- and X-class flares were selected. The time period during which the data were recorded spans from 2011 January to 2016 February. Of these events, approximately half are classified as white-light flares (WLFs), whereas the remaining events do not show any enhancements of the visible continuum (non-WLF; NWL). To determine the existence of WL emission, running difference images of not only the *Hinode*/ SOT WL (G-band, blue, green, and red filter) data, but also the *Solar Dynamics Observatory*/Helioseismic and Magnetic Imager continuum data are used. A comparison between these two groups of WL data in terms of duration, temperature, emission measure of *GOES* soft X-rays, distance between EUV flare ribbons, strength of hard X-rays, and photospheric magnetic field strength was undertaken. In this statistical study, WLF events are characterized by a shorter timescale and shorter ribbon distance compared with NWL events. From the scatter plots of the duration of soft X-rays and the energy of non-thermal electrons, a clear distinction between WLF and NWL events can be made. It is found that the precipitation of large amounts of accelerated electrons within a short time period plays a key role in generating WL enhancements. Finally, it was demonstrated that the coronal magnetic field strength in the flare region is one of the most important factors that allow the individual identification of WLF events from NWL events.

Key words: Sun: flares – Sun: particle emission – Sun: X-rays, gamma rays

1. Introduction

Solar flares are often associated with enhancements of visible continuum (white-light; WL) radiation. The first white-light flare (WLF) recorded was the Carrington flare of 1859 (Carrington 1859). WLFs are largely associated with energetic events such as *GOES* X-class flares and are rarely observed. However, using recent high-precision observations obtained from spacecraft (*Yohkoh*, *TRACE*, *Hinode*, etc.), WLFs have been observed in weaker flares such as *GOES* C-class flares (Matthews et al. 2003; Hudson et al. 2006; Jess et al. 2008; Wang 2009).

Although 150 years has passed since the discovery of WLF, the mechanism of WL emission is still not fully understood. One of the most famous correlations with WL emission is that of hard X-ray emission, which originates from accelerated electrons. Observationally, WL emission is well correlated with hard X-ray and radio emission, both in the time profile and emission location (e.g., Neidig 1989; Ding et al. 2003; Fletcher et al. 2007; Watanabe et al. 2010; Krucker et al. 2011; Kuhar et al. 2016). As a result there is some consensus that the origin of WL emission is non-thermal electrons. By comparing the total energy of WL and hard X-ray emission, the energy range characterizing WL emission can be estimated as a few tens of keVs (Neidig 1989; Fletcher et al. 2007; Watanabe et al. 2010; Kuhar et al. 2016). The total energy of the observed WL emission is therefore similar to the total energy of the accelerated electrons with energies typical of hard X-rays.

There are questions relating to the emission height of WLF. Theoretically, WL is emitted near the photosphere. However, non-thermal electrons in the energy range of 50–100 keV are almost thermalized by the time they reach the lower chromospheres, whereas hard X-rays are emitted from the lower chromosphere. To reach the photosphere, accelerated electrons need energies in excess of 900 keV (Neidig 1989). Even if such high-energy electrons exist, this is still not enough to explain the total energy of WL emission.

Observationally, the emission height of WL and hard X-rays and the relationship between them are measured by limb flares (e.g., Battaglia & Kontar 2011, 2012; Martínez Oliveros et al. 2012; Watanabe et al. 2013; Krucker et al. 2015). Some events show that WL emission takes place in the photosphere (Martínez Oliveros et al. 2012; Watanabe et al. 2013), whereas other events show that it occurs in the chromosphere (Battaglia & Kontar 2012; Krucker et al. 2015). Even in the same flare, different results were reported. For the 2011 February 24 flare, one paper reported there was a significant difference in source height between hard X-rays and WL (Battaglia & Kontar 2012), however, others showed no difference between them with a different analysis method (Martínez Oliveros et al. 2012). Determining the height of WL emission is therefore not a straightforward problem and at present its exact nature remains unsolved.

The emission height relationship between WL and hard X-rays reflects the emission mechanisms of WL emissions. Theories explaining WL emission mechanisms fall into two general categories, namely, one involves direct heating and the other indirect heating. A simple model for the direct heating case is that very high-energy (≫100 keV) electrons precipitate directly into the photosphere, thereby increasing the temperature of the photosphere and resulting in the emission of WL (Aboudarham & Henoux 1986; Neidig 1989). A further model involving the direct heating approach is that WL emission results from an optically thin source in the mid-chromosphere

that is directly heated by non-thermal electrons (Kerr & Fletcher 2014). An indirect heating model of WL emission may be outlined as follows: The WL emission region/layer differs from the energy deposition layer/region for non-thermal electrons. Relatively low-energy (<100 keV) electrons precipitate into the chromosphere wherein they dissipate energy. Energy is then transported from this heated region to the lower atmosphere. This energy transport is termed back-warming and the exact transport mechanism remains the topic of debate (Machado et al. 1989; Metcalf et al. 1990; Isobe et al. 2007). The resulting WL emission is thought to be caused by the photoionization of hydrogen atoms and recombination of associated photoelectrons. The excited neutral hydrogen atoms lead to Balmer Paschen continuum emission (Machado et al. 1986; Metcalf et al. 2003).

Although these emission mechanism models highlight the relationship between WL and hard X-ray emission, there are many flare events that do not have any WL enhancements even if they have hard X-ray emission. There are many reports of WLFs that discuss the correlation between hard X-rays and emission mechanisms. However, there are no studies that compare events without WL enhancements even if the flare itself is observed by continuum bands. To understand the conditions that produce enhancements of WL in solar flares, a statistical analysis was performed on WL data observed by the Solar Optical Telescope (SOT; Ichimoto et al. 2008; Shimizu et al. 2008; Suematsu et al. 2008; Tsuneta et al. 2008) on board *Hinode* and the Helioseismic and Magnetic Imager (HMI; Scherrer et al. 2012; Schou et al. 2012) on board *Solar Dynamics Observatory* (*SDO*; Pesnell et al. 2012). We compared these WL data with the data of the *GOES* soft X-rays, the *Reuven Ramaty High Energy Solar Spectroscopic Imager* (*RHESSI*; Lin et al. 2002) hard X-rays, and the strength of the photospheric magnetic fields, as observed by *SDO*/HMI. An investigation of the relationships between the many physical parameters recorded was completed and the results presented in this work provide some constraints on the mechanism of WL emission.

2. Event Selection

The *Hinode*/SOT provides high-resolution photometric and magnetic observations of various features in the photosphere and chromosphere and has the capability of observing WLFs. The broadband filtergraph imager on SOT contains interference filters to acquire images of the Ca II H (3968.5 Å, width 3 Å), G-band (4305.0 Å, width 8 Å), blue filter (4504.5 Å, width 4 Å), green filter (5550.5 Å, width 4 Å), and red filter (6684.0 Å, width 4 Å). From 2011, SOT performed a flare observation program that obtained continuum images of the G-band and the red, green, and blue filters when a solar flare was automatically detected (Kano et al. 2008) by the X-Ray Telescope (XRT; Golub et al. 2007) and the flare position was inside the SOTs field of view (FOV).

Not all flares are observed by SOT, due to restrictions related to SOTs FOV. Among the *Hinode* instruments, XRT has the capability to observe the full solar disk. SOT has a much smaller maximum FOV size of $328'' \times 164''$. Therefore, only flares that occur while *Hinode* is observing and are located inside the FOV may be observed by *Hinode*. It is important to determine which flares were observed by *Hinode* to analyze the flare data. Flare events that occurred while *Hinode* was observing were listed and checked to determine whether the event was inside the *Hinode* FOV. These results are available on the web site in the *Hinode* Flare Catalogue (Watanabe et al. 2012). In this catalog, the number of images obtained by the *Hinode* instruments is shown along with the *RHESSI* and Nobeyema radio heliograph information.

In this study, events were selected for the period 2011 January to 2016 February. To select flare events, the *Hinode* Flare Catalogue (Watanabe et al. 2012) was used. This catalog lists 11,387 flare events during the study period. M- and X-class flares were chosen for investigation because WLFs are usually associated with relatively large flares. Of the total 11,387 events, 721 events satisfied these selection criteria. From these 721 events, we selected those that were observed using *Hinode*/SOT in the visible continuum bands (G-band, blue, green, and red filters) during flare observation mode. This gave a revised total of 101 events. These 101 events were classified into WLF events and NWL events using running difference images in the SOT continuum data. The criterion for classification of WLF was the existence of WL enhancements under the Ca II H ribbon. All images through the flare evolution were searched for a WL signature. This resulted in the identification of 36 WLF events and 65 NWL events. However, it is possible that even if an event is classified as NWL from SOT data, WL emission may exist outside the SOTs FOV. To account for this factor, the *SDO*/HMI continuum data were checked and 13 further WLF events were identified (these WL enhancements were located on the 1600 Å ribbons). The final sample consisted of 49 WLF events (11 X-class and 38 M-class flares) and 52 NWL events (five X-class and 47 M-class flares). The event lists for WLF and NWL events are given in Tables 1 and 2, respectively. Statistical analysis was performed for the *Hinode*/SOT, *SDO*/HMI, and *GOES* data sets and the method of analysis and results are discussed in Sections 3.1–3.4.

Statistical analysis for the hard X-ray data observed by *RHESSI* was also performed. Among the 101 events, 27 were simultaneously observed with *RHESSI* and were shown to have greater than 50 keV emissions. Among them, 17 WLF events (six X-class and 11 M-class flares) and 10 NWL events (two X-class and nine M-class flares) were observed. An event list for the *RHESSI* data is available in Table 3. An analysis of hard X-ray data is described in Section 3.5.

3. Statistical Data Analyses

3.1. Flare Duration

In general, WL enhancements were found to be associated with large flares. However, some NWL events are associated with X-class flares. From these observational facts, it can be inferred that WLFs are associated with impulsive flares. Using this inference, correlations with flare duration were sought. The soft X-ray duration is easily obtained from *GOES* flare information (*GOES* flare start to end time). However, some flares occurred consecutively over a short time period and it was not possible to identify the start time and/or end time from soft X-ray light curves. It was therefore decided to use soft X-ray derivative data to determine flare duration. The soft X-ray derivative profile is almost the same as the hard X-ray profile from the Neupert effect (Neupert 1968). Although the Neupert effect is not always present for all flare events, this relationship was employed in this study because it is a very good index of flare duration.

Table 1
WLF Event List and Physical Parameters from *GOES* and *SDO* Data

GOES Flare Start YYYY/MM/DD hh:mm	GOES Derivative			GOES X-Ray Class	Sunspot Location	Derivative Duration (s)	@Derivative End Temperature (MK)	EM (10^49 cm^-3)	1600 Å Ribbon Distance (×10^3 km)	HMI Field Strength@1600 Å Ribbon	
	Start	Peak	End							Positive (G)	Negative (G)
2011 Feb 15 01:44	2011 Feb 15 01:45	2011 Feb 15 01:52	2011 Feb 15 01:56	X2.2	S20W10	631	21.3	9.85	12.0	572.4	−455.2
2011 Nov 03 20:16	2011 Nov 03 20:17	2011 Nov 03 20:21	2011 Nov 03 20:22	X1.9	N21E64	326	20.9	5.68	⋯	⋯	⋯
2012 Jan 27 17:37	2012 Jan 27 18:05	2012 Jan 27 18:26	2012 Jan 27 18:33	X1.7	N33W85	1676	16.0	8.88	⋯	⋯	⋯
2012 Jul 06 23:01	2012 Jul 06 23:03	2012 Jul 06 23:06	2012 Jul 06 23:08	X1.1	S13W59	307	20.0	5.07	38.6	131.6	−168.4
2012 Oct 23 03:13	2012 Oct 23 03:14	2012 Oct 23 03:15	2012 Oct 23 03:16	X1.8	S13E58	170	24.6	6.42	17.5	460.9	−488.9
2014 Oct 22 14:02	2014 Oct 22 14:02	2014 Oct 22 14:03	2014 Oct 22 14:17	X1.6	S14E13	850	20.2	5.99	22.1	533.8	−759.8
2014 Oct 24 20:50	2014 Oct 24 21:06	2014 Oct 24 21:15	2014 Oct 24 21:19	X3.1	S16W21	783	22.3	9.00	34.3	466.9	−557.0
2014 Oct 26 10:04	2014 Oct 26 10:35	2014 Oct 26 10:44	2014 Oct 26 10:54	X2.0	S18W40	1155	21.2	8.41	51.1	443.9	−942.0
2014 Oct 27 14:12	2014 Oct 27 14:10	2014 Oct 27 14:26	2014 Oct 27 14:31	X2.0	S17W52	1237	20.9	6.72	81.4	363.0	−552.5
2014 Dec 20 00:11	2014 Dec 20 00:14	2014 Dec 20 00:21	2014 Dec 20 00:25	X1.8	S21W24	702	18.9	8.05	51.8	457.0	−318.8
2015 Mar 11 16:11	2015 Mar 11 16:13	2015 Mar 11 16:19	2015 Mar 11 16:21	X2.1	S17E22	512	21.5	9.38	18.2	627.8	−606.4
2011 Feb 14 17:20	2011 Feb 14 17:23	2011 Feb 14 17:24	2011 Feb 14 17:26	M2.2	S20W04	183	15.4	1.22	8.9	429.2	−140.8
2011 Feb 18 09:55	2011 Feb 18 10:07	2011 Feb 18 10:10	2011 Feb 18 10:11	M6.6	S21W55	233	20.4	3.25	13.8	386.9	−242.4
2011 Feb 18 12:59	2011 Feb 18 13:00	2011 Feb 18 13:02	2011 Feb 18 13:03	M1.4	S21W55	196	16.2	0.78	16.2	565.5	−225.3
2011 Sep 28 13:24	2011 Sep 28 13:25	2011 Sep 28 13:26	2011 Sep 28 13:28	M1.2	N11E00	168	15.6	0.69	⋯	⋯	⋯
2011 Nov 02 21:52	2011 Nov 02 21:53	2011 Nov 02 21:57	2011 Nov 02 22:00	M4.3	N20E77	422	17.9	2.05	⋯	⋯	⋯
2011 Dec 31 13:09	2011 Dec 31 13:11	2011 Dec 31 13:13	2011 Dec 31 13:15	M2.4	S25E46	254	17.4	1.21	10.7	425.1	−339.9
2012 Mar 06 12:23	2012 Mar 06 12:39	2012 Mar 06 12:40	2012 Mar 06 12:41	M2.1	N21E40	88	16.0	1.15	12.8	362.1	−392.8
2012 Mar 06 21:04	2012 Mar 06 21:09	2012 Mar 06 21:10	2012 Mar 06 21:11	M1.3	N16E30	67	16.1	0.73	4.4	451.4	−687.6
2012 May 09 12:21	2012 May 09 12:27	2012 May 09 12:29	2012 May 09 12:32	M4.7	N13E31	268	18.4	2.28	11.8	275.4	−212.2
2012 May 09 21:01	2012 May 09 21:01	2012 May 09 21:03	2012 May 09 21:05	M4.1	N12E26	203	18.8	1.91	16.3	299.9	−393.8
2012 May 10 20:20	2012 May 10 20:21	2012 May 10 20:25	2012 May 10 20:26	M1.7	N12E12	263	15.6	0.95	7.5	282.0	−267.2
2012 Jul 05 03:25	2012 Jul 05 03:34	2012 Jul 05 03:35	2012 Jul 05 03:36	M4.7	S18W29	90	18.8	2.27	4.4	547.5	−421.1
2012 Jul 05 21:37	2012 Jul 05 21:44	2012 Jul 05 21:45	2012 Jul 05 21:45	M1.6	S12W46	47	13.4	1.02	48.2	38.3	−136.8
2012 Jul 06 01:37	2012 Jul 06 01:37	2012 Jul 06 01:38	2012 Jul 06 01:40	M2.9	S18W41	156	17.7	1.46	13.6	556.3	−357.1
2012 Jul 08 12:05	2012 Jul 08 12:08	2012 Jul 08 12:09	2012 Jul 08 12:10	M1.4	S21W69	106	16.5	0.73	⋯	⋯	⋯
2013 Jun 07 22:11	2013 Jun 07 22:33	2013 Jun 07 22:43	2013 Jun 07 22:48	M5.9	S32W89	880	18.9	2.69	⋯	⋯	⋯
2013 Oct 26 19:24	2013 Oct 26 19:23	2013 Oct 26 19:24	2013 Oct 26 19:27	M3.1	S09E81	203	14.5	1.72	⋯	⋯	⋯
2013 Oct 28 15:07	2013 Oct 28 15:09	2013 Oct 28 15:10	2013 Oct 28 15:14	M4.4	S06E28	315	14.6	2.39	17.3	443.2	−397.2
2013 Dec 22 14:45	2013 Dec 22 15:07	2013 Dec 22 15:10	2013 Dec 22 15:12	M3.3	S19W56	278	15.6	1.80	15.9	334.4	−223.1
2013 Dec 23 08:59	2013 Dec 23 09:04	2013 Dec 23 09:06	2013 Dec 23 09:06	M1.6	S17W63	129	16.1	0.86			
2013 Dec 31 21:45	2013 Dec 31 21:47	2013 Dec 31 21:52	2013 Dec 31 21:57	M6.4	S16W35	584	17.9	3.06	30.9	409.1	−358.2
2014 Jan 01 18:40	2014 Jan 01 18:41	2014 Jan 01 18:47	2014 Jan 01 18:51	M9.9	S14W47	612	16.1	4.99	7.3	140.5	−147.2
2014 Mar 13 19:03	2014 Mar 13 19:10	2014 Mar 13 19:12	2014 Mar 13 19:17	M1.2	N15W87	408	13.5	0.72			
2014 Oct 21 13:35	2014 Oct 21 13:36	2014 Oct 21 13:37	2014 Oct 21 13:37	M1.2	S14E35	74	14.0	0.87	11.3	122.7	−174.1
2014 Oct 22 01:16	2014 Oct 22 01:36	2014 Oct 22 01:46	2014 Oct 22 01:49	M8.7	S13E21	733	19.7	3.41	73.2	317.5	−843.2
2014 Nov 05 09:26	2014 Nov 05 09:38	2014 Nov 05 09:42	2014 Nov 05 09:46	M7.9	N20E68	514	18.7	3.68	⋯	⋯	⋯
2014 Nov 15 11:40	2014 Nov 15 11:48	2014 Nov 15 11:58	2014 Nov 15 12:02	M3.2	S09E63	866	16.2	1.65	⋯	⋯	⋯
2014 Nov 15 20:38	2014 Nov 15 20:40	2014 Nov 15 20:43	2014 Nov 15 20:45	M3.7	S13E63	322	16.0	1.93	⋯	⋯	⋯
2015 Jan 13 04:13	2015 Jan 13 04:15	2015 Jan 13 04:21	2015 Jan 13 04:24	M5.6	N06W70	528	16.2	2.89	⋯	⋯	⋯
2015 Mar 12 04:41	2015 Mar 12 04:41	2015 Mar 12 04:43	2015 Mar 12 04:45	M3.2	S15E11	246	19.0	1.51	28.0	292.4	−369.0
2015 Mar 12 21:44	2015 Mar 12 21:46	2015 Mar 12 21:48	2015 Mar 12 21:50	M2.7	S15E01	252	18.0	1.34	9.7	258.2	−352.4
2015 Mar 15 09:36	⋯	⋯	⋯	M1.0	S20W24	⋯	⋯	⋯	⋯	⋯	⋯

4

Table 1
(Continued)

GOES Flare Start YYYY/MM/DD hh:mm	GOES Derivative			GOES X-Ray Class	Sunspot Location	Derivative Duration (s)	@Derivative End		1600 Å Ribbon Distance (×10³ km)	HMI Field Strength@1600 Å Ribbon	
	Start	Peak	End				Temperature (MK)	EM (10⁴⁹ cm⁻³)		Positive (G)	Negative (G)
2015 Jun 22 17:23	2015 Jun 22 17:49	2015 Jun 22 17:58	2015 Jun 22 18:00	M6.5	N12W08	639	19.1	2.38	24.7	520.0	−511.8
2015 Jun 25 08:02	2015 Jun 25 08:04	2015 Jun 25 08:14	2015 Jun 25 08:14	M7.9	N09W42	594	18.3	2.66	13.7	242.7	−190.5
2015 Sep 29 19:08	2015 Sep 29 19:22	2015 Sep 29 19:23	2015 Sep 29 19:24	M1.1	S20W36	117	12.5	0.76	16.3	75.5	−77.8
2015 Sep 30 13:14	2015 Sep 30 13:18	2015 Sep 30 13:19	2015 Sep 30 13:20	M1.1	S23W59	62	15.8	0.74	6.2	221.2	−156.9
2015 Oct 01 13:03	2015 Oct 01 13:05	2015 Oct 01 13:09	2015 Oct 01 13:10	M4.5	S23W64	311	17.9	2.27	⋯	⋯	⋯
2015 Oct 02 00:06	2015 Oct 02 00:07	2015 Oct 02 00:10	2015 Oct 02 00:13	M5.5	S19W67	349	18.1	2.71	⋯	⋯	⋯

Table 2
NWL Event List and Physical Parameters from *GOES* and *SDO* Data

GOES Flare Start YYYY/MM/DD hh:mm	GOES Derivative Start	GOES Derivative Peak	GOES Derivative End	GOES X-Ray Class	Sunspot Location	Derivative Duration (s)	@Derivative End Temperature (MK)	@Derivative End EM (10^{49} cm^{-3})	1600 Å Ribbon Distance ($\times 10^3$ km)	HMI Field Strength @1600 Å Ribbon Positive (G)	HMI Field Strength @1600 Å Ribbon Negative (G)
2012 Mar 05 02:30	2012 Mar 05 03:30	2012 Mar 05 03:45	2012 Mar 05 03:55	X1.1	N19E58	1483	18.7	4.55	33.0	539.2	−523.3
2012 Jul 12 15:37	2012 Jul 12 16:11	2012 Jul 12 16:32	2012 Jul 12 16:44	X1.4	S13W03	2011	17.9	6.47	46.7	975.8	−436.5
2013 May 15 01:24	2013 May 15 01:25	2013 May 15 01:43	2013 May 15 01:48	X1.2	N12E64	1366	16.3	6.57	⋯	⋯	⋯
2014 Oct 25 16:55	2014 Oct 25 16:47	2014 Oct 25 17:03	2014 Oct 25 17:07	X1.0	S10W22	1214	19.8	4.79	40.4	521.6	−383.5
2014 Nov 07 16:53	2014 Nov 07 17:17	2014 Nov 07 17:22	2014 Nov 07 17:25	X1.6	N14E36	475	17.5	7.83	26.6	399.4	−413.7
2011 Feb 16 07:35	2011 Feb 16 07:37	2011 Feb 16 07:40	2011 Feb 16 07:43	M1.1	S19W29	358	16.1	0.58	23.3	521.3	−519.7
2011 Sep 23 21:54	2011 Sep 23 21:59	2011 Sep 23 22:03	2011 Sep 23 22:10	M1.6	N12E56	700	13.3	0.88	58.2	274.8	−890.5
2011 Nov 03 10:58	2011 Nov 03 10:59	2011 Nov 03 11:07	2011 Nov 03 11:10	M2.5	N20E70	647	16.8	1.26	⋯	⋯	⋯
2011 Nov 05 03:08	2011 Nov 05 03:29	2011 Nov 05 03:30	2011 Nov 05 03:32	M3.7	N20E47	197	14.9	2.00	27.3	492.4	−345.4
2011 Nov 05 20:31	2011 Nov 05 20:33	2011 Nov 05 20:35	2011 Nov 05 20:37	M1.8	N21E37	258	17.2	0.89	11.5	391.1	−327.5
2011 Dec 31 16:16	2011 Dec 31 16:21	2011 Dec 31 16:24	2011 Dec 31 16:25	M1.5	S25E42	262	15.6	0.85	27.1	248.6	−353.7
2012 Jan 17 04:41	2012 Jan 17 04:43	2012 Jan 17 04:45	2012 Jan 17 04:52	M1.0	N18E53	547	13.8	0.59	11.3	199.2	−140.5
2012 Jan 18 19:04	2012 Jan 18 19:06	2012 Jan 18 19:09	2012 Jan 18 19:11	M1.7	N17E32	305	14.6	0.91	11.1	⋯	⋯
2012 May 07 14:03	2012 May 07 14:05	2012 May 07 14:19	2012 May 07 14:26	M1.9	S20W49	1224	14.1	1.00	41.1	166.8	−241.4
2012 May 09 14:02	2012 May 09 14:04	2012 May 09 14:06	2012 May 09 14:08	M1.8	N06E22	280	14.8	1.04	20.7	223.2	−594.1
2012 Jun 13 11:29	⋯	⋯	⋯	M1.2	S16E18	⋯	⋯	⋯	⋯	⋯	
2012 Jul 06 08:17	2012 Jul 06 08:18	2012 Jul 06 08:22	2012 Jul 06 08:23	M1.5	S17W40	319	15.4	0.84	13.7	809.5	−291.3
2012 Jul 14 04:51	2012 Jul 14 04:51	2012 Jul 14 04:54	2012 Jul 14 04:58	M1.0	S22W36	366	13.8	0.59	44.8	575.1	−623.0
2013 May 02 04:58	2013 May 02 04:59	2013 May 02 05:04	2013 May 02 05:08	M1.1	N10W26	553	13.8	0.61	23.4	341.9	−116.9
2013 May 03 16:39	2013 May 03 16:40	2013 May 03 16:46	2013 May 03 16:49	M1.3	N10W38	529	13.1	0.72	15.0	140.5	−166.1
2013 Aug 17 18:16	2013 Aug 17 18:19	2013 Aug 17 18:22	2013 Aug 17 18:23	M3.3	S07W30	275	16.5	1.74	7.9	386.8	−260.6
2013 Oct 22 00:14	2013 Oct 22 00:15	2013 Oct 22 00:18	2013 Oct 22 00:21	M1.0	N06E17	356	15.0	0.55	25.3	390.9	−490.7
2013 Oct 28 14:46	2013 Oct 28 14:55	2013 Oct 28 14:59	2013 Oct 28 15:00	M2.7	S08E28	286	16.6	1.22	4.5	318.6	−221.2
2013 Dec 07 07:17	2013 Dec 07 07:19	2013 Dec 07 07:22	2013 Dec 07 07:28	M1.2	S16W49	522	12.0	0.81	34.1	117.2	−171.1
2013 Dec 22 08:05	2013 Dec 22 08:07	2013 Dec 22 08:09	2013 Dec 22 08:11	M1.9	S20W49	235	16.5	0.99	28.2	365.2	−183.4
2014 Jan 04 10:16	2014 Jan 04 10:18	2014 Jan 04 10:20	2014 Jan 04 10:24	M1.3	S05E48	350	14.2	0.74	47.3	136.1	−240.2
2014 Jan 04 19:05	2014 Jan 04 19:04	2014 Jan 04 19:15	2014 Jan 04 19:28	M4.0	S11E34	1450	14.7	1.87	109.7	⋯	⋯
2014 Feb 14 02:40	2014 Feb 14 02:47	2014 Feb 14 02:54	2014 Feb 14 02:56	M2.3	S12W25	547	15.3	1.24	16.4	390.8	−275.7
2014 Feb 14 12:29	2014 Feb 14 12:30	2014 Feb 14 12:39	2014 Feb 14 12:40	M1.6	S15W36	580	14.0	0.91	30.9	138.5	−118.4
2014 Jun 12 21:34	2014 Jun 12 21:40	2014 Jun 12 21:57	2014 Jun 12 22:03	M3.1	S20W55	1413	13.7	1.37	65.9	589.9	−180.8
2014 Jun 15 23:50	2014 Jun 15 23:52	2014 Jun 15 23:56	2014 Jun 15 23:59	M1.0	S19E08	432	12.1	0.62	36.3	121.8	−187.4
2014 Aug 01 17:55	2014 Aug 01 17:56	2014 Aug 01 18:00	2014 Aug 01 18:05	M1.5	S10E11	543	12.2	0.84	39.0	388.6	−146.5
2014 Oct 26 19:59	2014 Oct 26 19:58	2014 Oct 26 20:05	2014 Oct 26 20:12	M2.4	S15W45	848	16.7	1.06	107.0	315.0	−768.5
2014 Oct 28 02:15	2014 Oct 28 02:11	2014 Oct 28 02:37	2014 Oct 28 02:39	M3.4	S14W61	1685	16.0	1.75	⋯	⋯	⋯
2014 Oct 29 09:54	2014 Oct 29 09:55	2014 Oct 29 09:58	2014 Oct 29 10:01	M1.2	S18W77	365	14.4	0.69	⋯	⋯	⋯
2014 Nov 05 18:50	2014 Nov 05 19:24	2014 Nov 05 19:31	2014 Nov 05 19:39	M2.9	N17E65	900	15.0	1.48	⋯	⋯	⋯
2014 Nov 07 02:01	2014 Nov 07 02:39	2014 Nov 07 02:42	2014 Nov 07 02:46	M2.7	N17E50	452	16.2	1.34	28.9	564.0	−427.6
2014 Nov 07 09:43	2014 Nov 07 10:13	2014 Nov 07 10:17	2014 Nov 07 10:21	M1.0	N15E43	428	14.3	0.55	9.7	317.4	−267.6
2014 Dec 04 07:36	2014 Dec 04 08:01	2014 Dec 04 08:05	2014 Dec 04 08:08	M1.3	S24W27	403	13.9	0.69	17.7	470.3	−177.8
2014 Dec 05 11:33	⋯	⋯	⋯	M1.5	S23W41	⋯	⋯	⋯	⋯	⋯	⋯
2014 Dec 19 09:31	2014 Dec 19 09:33	2014 Dec 19 09:39	2014 Dec 19 09:43	M1.3	S19W27	619	13.1	0.79	31.3	244.1	−219.3
2015 Mar 12 12:09	2015 Mar 12 12:08	2015 Mar 12 12:11	2015 Mar 12 12:13	M1.4	S18E05	314	12.3	0.90	68.5	481.5	−380.5
2015 Mar 12 13:45	2015 Mar 12 14:02	2015 Mar 12 14:04	2015 Mar 12 14:08	M4.2	S15E06	361	17.4	2.07	24.0	417.0	−298.8

6

Table 2
(Continued)

GOES Flare Start YYYY/MM/DD hh:mm	GOES Derivative			GOES X-Ray Class	Sunspot Location	Derivative Duration (s)	@Derivative End		1600 Å Ribbon Distance (×10³ km)	HMI Field Strength @1600 Å Ribbon	
	Start	Peak	End				Temperature (MK)	EM (10⁴⁹ cm⁻³)		Positive (G)	Negative (G)
2015 Mar 13 05:49	2015 Mar 13 06:00	2015 Mar 13 06:03	2015 Mar 13 06:07	M1.8	S14W02	385	16.0	0.96	10.4	317.5	−400.0
2015 Mar 14 04:23	2015 Mar 14 04:33	2015 Mar 14 04:36	2015 Mar 14 04:40	M1.3	S14W12	383	14.4	0.77	39.8	144.4	−655.1
2015 Mar 15 22:42	2015 Mar 15 22:45	2015 Mar 15 22:46	2015 Mar 15 22:47	M1.2	S19W32	131	14.2	0.20	55.0	304.0	−586.6
2015 Mar 16 10:39	2015 Mar 16 10:41	2015 Mar 16 10:50	2015 Mar 16 10:56	M1.6	S17W39	876	15.1	0.86	28.9	165.5	−342.2
2015 Mar 17 22:49	2015 Mar 17 23:28	2015 Mar 17 23:30	2015 Mar 17 23:32	M1.0	S21W56	270	12.0	0.66	43.4	107.7	−106.4
2015 Jun 21 01:02	2015 Jun 21 01:22	2015 Jun 21 01:27	2015 Jun 21 01:37	M2.0	N12E13	895	15.2	0.94	29.3	803.1	−681.8
2015 Aug 30 02:01	2015 Aug 30 02:54	2015 Aug 30 02:56	2015 Aug 30 03:01	M1.4	S17W80	445	13.9	0.61	⋯	⋯	⋯
2015 Sep 27 20:54	2015 Sep 27 20:55	2015 Sep 27 20:57	2015 Sep 27 21:00	M1.0	S21W16	287	14.6	0.57	10.8	378.9	−286.7
2016 Jan 01 23:10	2016 Jan 01 23:30	2016 Jan 01 23:37	2016 Jan 01 23:44	M2.3	S25W82	811	13.0	0.95	⋯	⋯	⋯

Table 3
WLF and NWL Event List and Physical Parameters from *RHESSI* Data

GOES Flare Start YYYY/MM/DD hh:mm	*GOES* X-Ray Class	Sunspot Location	Derivative Duration (s)	50–100 keV HXR Peak (counts s^{-1} cm^{-2} keV^{-1})	Power-law Index	Energy Deposition Rate (>30 keV) (erg s^{-1})
NWL events						
2013 May 15 01:24	X1.2	N12E64	1366	0.53	−3.2	3.09E+27
2014 Oct 25 16:55	X1.0	S10W22	1214	0.07	−8.3	5.97E+28
2011 Dec 31 16:16	M1.5	S25E42	262	0.12	−2.7	2.56E+26
2013 May 02 04:58	M1.1	N10W26	553	0.67	−2.8	1.02E+27
2013 May 03 16:39	M1.3	N10W38	529	0.12	−3.9	8.04E+26
2013 Oct 22 00:14	M1.0	N06E17	356	0.06	−4.5	5.46E+26
2013 Dec 22 08:05	M1.9	S20W49	235	0.07	−2.0	3.58E+25
2014 Jan 04 10:16	M1.3	S05E48	350	0.15	−3.6	1.28E+27
2014 Feb 14 12:29	M1.6	S15W36	580	0.04	−2.4	6.20E+25
2015 Mar 15 22:42	M1.2	S19W32	131	0.21	−6.6	4.35E+25
WLF events						
2011 Feb 15 01:44	X2.2	S20W10	631	0.74	−4.3	1.34E+28
2012 Oct 23 03:13	X1.8	S13E58	170	7.67	−3.1	3.66E+28
2014 Oct 22 14:02	X1.6	S14E13	850	2.93	−4.7	9.36E+28
2014 Oct 24 20:50	X3.1	S16W21	783	1.03	−5.9	1.06E+29
2014 Oct 27 14:12	X2.0	S17W52	1237	0.26	−6.2	3.85E+28
2015 Mar 11 16:11	X2.1	S17E22	512	64.2	−7.1	3.77E+28
2011 Feb 18 09:55	M6.6	S21W55	233	0.43	−3.0	1.84E+27
2011 Dec 31 13:09	M2.4	S25E46	254	0.11	−3.4	3.97E+26
2012 May 09 12:21	M4.7	N13E31	268	0.12	−3.4	7.44E+26
2012 May 10 20:20	M1.7	N12E12	263	0.20	−4.6	5.10E+27
2012 Jul 05 03:25	M4.7	S18W29	90	0.34	−4.7	3.16E+27
2012 Jul 06 01:37	M2.9	S18W41	156	1.27	−3.3	4.18E+27
2013 Oct 28 15:07	M4.4	S06E28	315	0.18	−3.3	1.14E+27
2013 Dec 22 14:45	M3.3	S19W56	278	0.08	−3.1	3.47E+26
2014 Oct 22 01:16	M8.7	S13E21	733	2.15	−3.7	2.38E+28
2015 Mar 12 04:41	M3.2	S15E11	246	1.02	−5.1	1.20E+28
2015 Mar 12 21:44	M2.7	S15E01	252	0.47	−4.5	6.92E+27

Figure 1 shows sample light curves of *GOES* soft X-ray flux and their time derivative. The left panels show an X2.1-class flare on 2015 March 11 as a sample of impulsive flare. The right panels show an X1.4-class flare on 2012 July 12 as a sample of long duration event. Flare duration for the X1.4 flare was four times longer than that of the X2.1 flare. From these soft X-ray derivative data, the derivative start, peak, and end time and derivative duration were obtained, as shown in Tables 1 and 2. The derivative peak time is defined as the time of the peak in derivative data from the start of the *GOES* flare to its peak. The derivative start time is defined as the time when the derivative data has a continuous positive value till the derivative peak. The derivative end time is defined as the time from the first negative value from the derivative peak time. In some events (flares on 2012 June 13, 2014 December 05, and 2015 March 15), no *GOES* data could be obtained and so no derivative data information appears in Tables 1 and 2.

The relationship between the *GOES* soft X-ray peak flux and the derivative duration is shown in the left-hand side panel of Figure 2. WLF events (represented by blue diamonds) show shorter duration compared with NWL events (represented by red crosses). It appears that the flare derivative duration is roughly correlated with the *GOES* soft X-ray flux. As a result, the average of both groups could not be compared directly. The average duration of WLF events was 419 s, whereas the average duration for NWL events was 619 s. The average duration of NWL events is therefore 1.5 times longer than that of WLF events.

Because there is a relationship between the *GOES* X-ray peak flux and the flare derivative duration, the *GOES* X-ray peak flux was divided by the derivative duration and this number was used to represent the impulsivity of the flare. This impulsivity reflects the increase in rate of hard X-ray emission. If there are *RHESSI* data for all flare events, we do not need to use the *GOES* X-ray derivative data, only the one-third of flare events were observed by *RHESSI* in fact, so we used this method. The right-hand side panel of Figure 2 shows a histogram of flare impulsivity. Figure 2 clearly shows two separate peaks, namely, WLF events (blue), which exhibit a shorter duration and larger flare class (impulsive flare) compared with NWL events (red). This result indicates that the impulsivity of the flare is one of the causative factors of WL enhancement.

3.2. Temperature and Emission Measure

The temperature and emission measure of each flare was calculated using the CHIANTI model. These values were measured at the derivative end time because this time characterizes the end of the energy release from the flare. Figure 3 is a scatter plot of the temperature and emission measure for all events and this graphically indicates there is a positive correlation between these two parameters. The relationship between the emission measure and electron temperature has been reported by Shibata & Yokoyama (1999, 2002). Figure 2 in Shibata & Yokoyama (2002) shows four theoretical curves for coronal magnetic field strengths of 5,
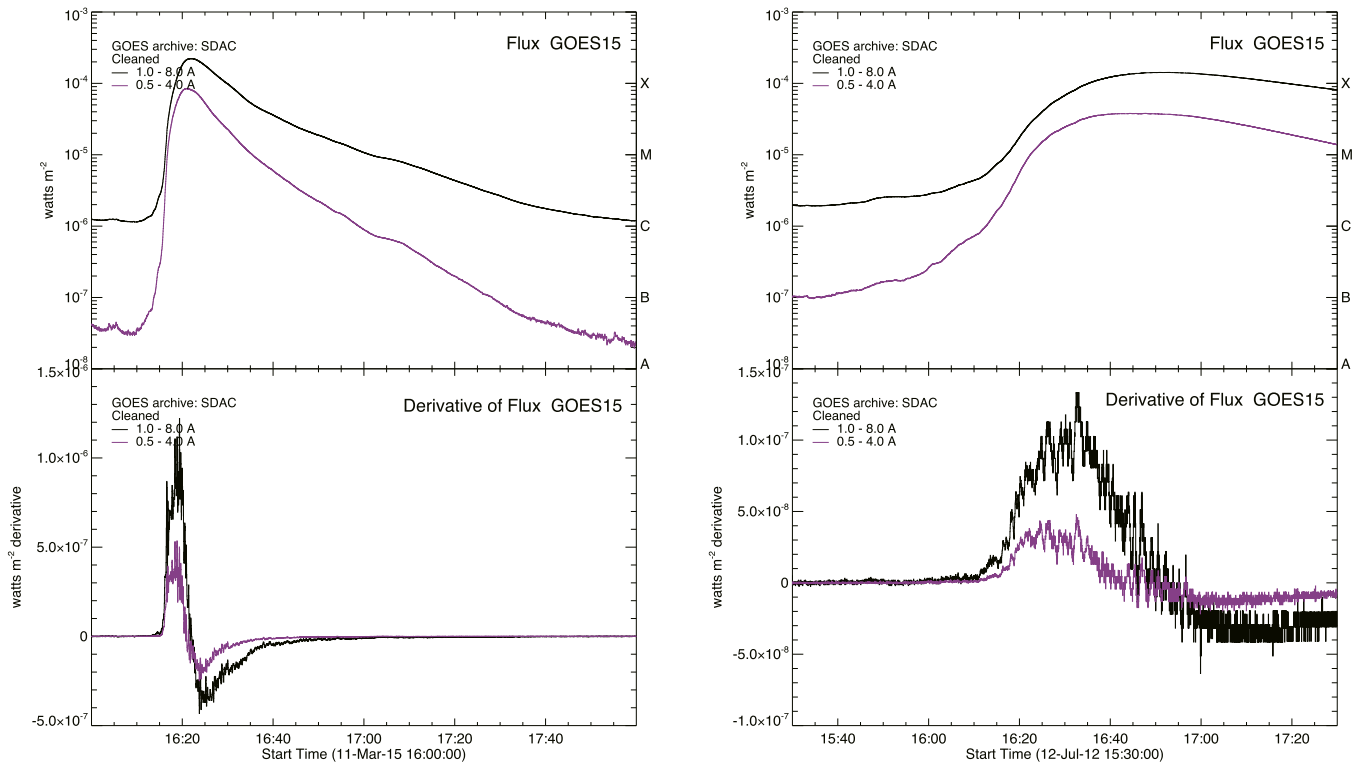
Figure 1. Sample light curves of *GOES* soft X-ray flux and their derivative of flux. Left: *GOES* soft X-ray light curve (top) of the X2.1 flare on 2015 March 11 for the sample of impulsive flare and its time derivative (bottom). Right: *GOES* soft X-ray light curve (top) of the X1.4 flare on 2012 July 12 for the sample of non-impulsive flare and its time derivative (bottom).

15, 50, and 150 G at the energy-release site of the flare. When this figure is compared with Figure 3 presented in this study, it can be observed that WLF and NWL events are located within the solar flare region. It can be seen that WLF events (represented by blue diamonds) are distributed toward the right-hand side of the plot, whereas NWL events (represented by red crosses) are located on the left-hand side of the plot. Four theoretical curves with magnetic field strength $B = 50, 60, 70, 80$ G are also plotted in Figure 3. Inspection of the $B = 70$ G curve indicates that 41 NWL events (82% of the NWL events) are located on the left-hand side of Figure 3 (region of weak coronal magnetic field strength) and 31 WLF events (65% of the WLF events) are located on the right-hand side of Figure 3 (region of strong coronal magnetic field strength). The difference in the distribution of these data may be due to differences in the coronal magnetic field strength at the site of the energy release. This result suggests that there is a tendency of the coronal magnetic field is weaker for NWL events than for WLF events.

3.3. Distance of Flare Ribbons

The distance of flare ribbons is measured to obtain the difference between the flare formal size for WLF and NWF events. To determine flare ribbons, the 1600 Å UV emission of the Atmospheric Imaging Assembly (AIA; Lemen et al. 2012) on board *SDO* was used. From the two flare ribbons observed, the brightest point of each ribbon at the corresponding *GOES* soft X-ray derivative peak time was determined and the separation between the brightest points was calculated. Among all the events listed in Tables 1 and 2, flare ribbon distance for three events could not be determined due to lack of *GOES*

derivative data. Furthermore, limb flares over E60 or W60 were removed from this analysis. The *SDO* data for the 2011 September 28 event were found to be missing, so these data were also not included in this analysis. Data were corrected for the effect of parallax to determine flare location.

The left-hand side panel of Figure 4 shows the relationship between the separation of the two flare ribbons and *GOES* soft X-ray class. It appears that there is a rough correlation between the ribbon distance and soft X-ray class, i.e., intense flares have a relatively large size. However, the ribbon distance of NWL events is located in the upper part of the left-hand side panel of Figure 4 compared with that of WLF events. The average separation for WLF events was determined as 2.2×10^3 km and that for NWL events as 3.3×10^3 km. The separation of WLF events is therefore significantly less than that of NWL events. This result indicates that the flare formal size of WLF events is relatively more compact than that of NWL events.

This flare ribbon distance is an index of flare size. When the emission measure is divided by flare volume (distance^3) and the square root taken, an index of flare loop density can be obtained. The right-hand side panel of Figure 4 shows the histogram of event number for flare density. In this figure, it is just possible to see two peaks for WLF events (blue) and for NWL events (red). This result indicates that the plasma density of the flare is one of the causative factors of WL enhancement.

3.4. Field Strength Under the Flare Ribbons

From Section 3.2, it was suggested that there is a relationship between WLF and NWL events and the coronal magnetic field strength. However, no coronal magnetic field strength data exist in the observational data used in this study. Instead, the
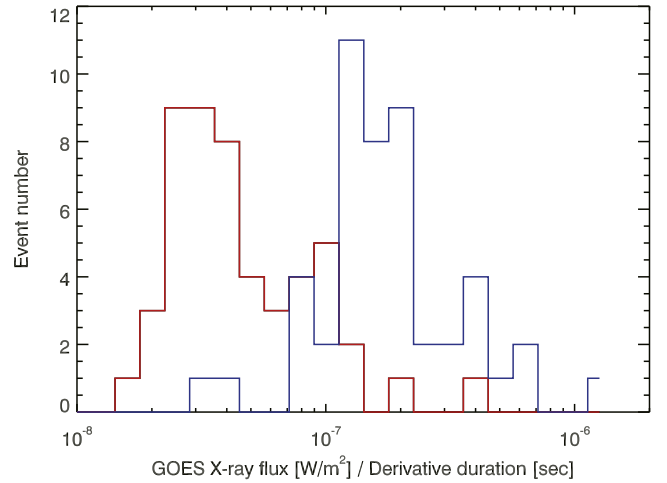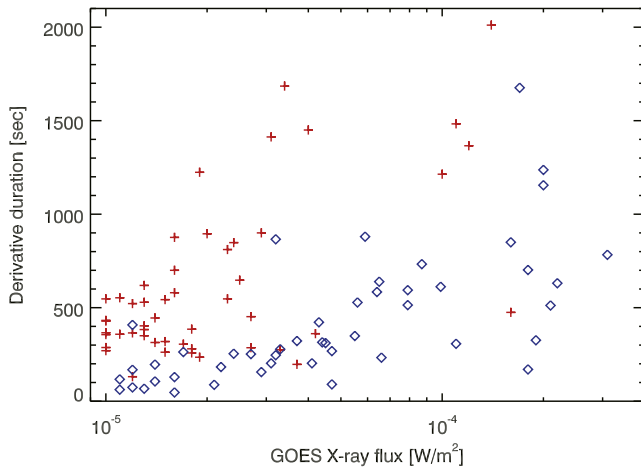
Figure 2. Left: the relationship between the *GOES* soft X-ray peak flux and the derivative duration as estimated from *GOES* X-ray data. The diamond (blue) and cross (red) symbols correspond to WLF and NWL events, respectively. Right: histogram of event number of flare impulsivity.
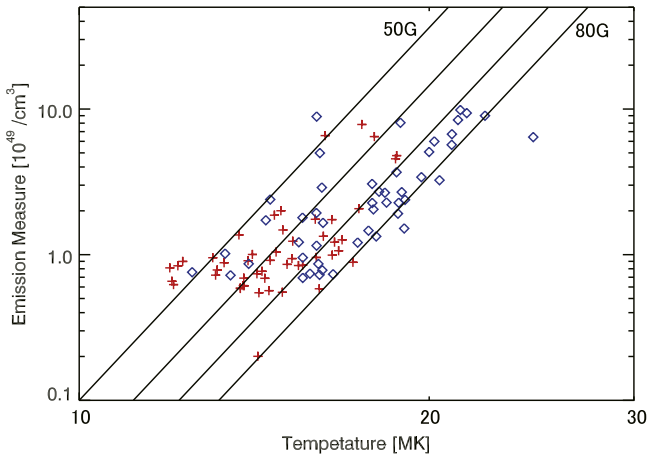
Figure 3. Scatter plot of temperature and emission measure at the derivative peak, as determined from the *GOES* soft X-ray data. The diamond (blue) and cross (red) symbols correspond to WLF and NWL events, respectively. Both axes are represented using a log scale. The relationship between emission measure and temperature based on Shibata & Yokoyama (1999, 2002) is superposed for values of $B = 50, 60, 70,$ and 80 G.

photospheric magnetic field strength under the flare ribbons as obtained in Section 3.3 is employed.

The *SDO*/HMI field strength data under the 1600 Å flare ribbons is therefore used in this analysis. For the two flare ribbons associated with each flare, positive field strength is taken from one flare ribbon and negative field strength taken from the other ribbon. Most of the event, these flare ribbons were located on the plage region, not umbrae. We calculated the average field strength under the 1600 Å flare ribbons.

Figure 5 shows the relationship between the *GOES* soft X-ray peak flux and the field strength under the 1600 Å flare ribbons as estimated from *SDO*/HMI data (taken from around the derivative peak time of *GOES* soft X-ray data). Unfortunately, there was a high degree of scatter in the data and no relationship could be determined between these two parameters.

3.5. Hard X-Ray Data Analysis

As mentioned in Section 2, a statistical analysis of hard X-ray data as observed by *RHESSI* was performed. Among the

101 *Hinode*/SOT events, 46 flare events were simultaneously observed with *RHESSI* . Among the 46 flare events, 21 events were associated with the WLF events and 25 events were the result of NWL events. Among them, 17 WLF events (6 X-class and 11 M-class flares) and 10 NWL events (2 X-class and 9 M-class flares) have emission greater than 50 keV. Physical parameters for these events are given in Table 3. Based on these events, hard X-ray photon counts and spectra could be analyzed.

3.5.1. Maximum Photon Counts of Hard X-rays

The maximum photon count of 50–100 keV hard X-ray photons during the flares was investigated. The photon count of each flare is given in Table 3. A scatter plot of the photon count and *GOES* soft X-ray flux is shown in Figure 6. Consideration of Figure 6 shows that hard X-ray photon count is roughly correlated with the *GOES* soft X-ray flux. The average photon count of the hard X-rays was calculated and found to be approximately 4.6 counts s^{-1} cm^{-2} keV^{-1} for WLF events and 0.2 counts s^{-1} cm^{-2} keV^{-1} for NWL events. Although the standard deviation is larger than the above mentioned values, the maximum photon count of WLF events is significantly larger than that of NWL events. This is directly related to the fact that the *GOES* soft X-ray flux for WLF events is larger than that for NWL events.

3.5.2. Hard X-Ray Spectra and Non-thermal Energy

Spectral fitting was performed for 27 events using a single power law to describe each hard X-ray spectrum in the region of the hard X-ray peak time and in the range of 30–100 keV. Indices for the power laws obtained are given in Table 3 and the correlation of spectral index and *GOES* soft X-ray flux are given in Figure 7. The average power-law indices are −4.3 for WLF events and −4.0 for NWL events. Because the standard deviation is smaller than − 1.0, there is no significant difference in the power-law indices.

The deposition rate of non-thermal energy was then calculated assuming a thick target model with a low-energy cutoff of 30 keV (Brown 1971). This was done using the same method as described in Watanabe et al. (2010). The calculated deposition rate of the non-thermal energy and *GOES* soft X-ray flux are given in Table 3. The corresponding scatter plot is
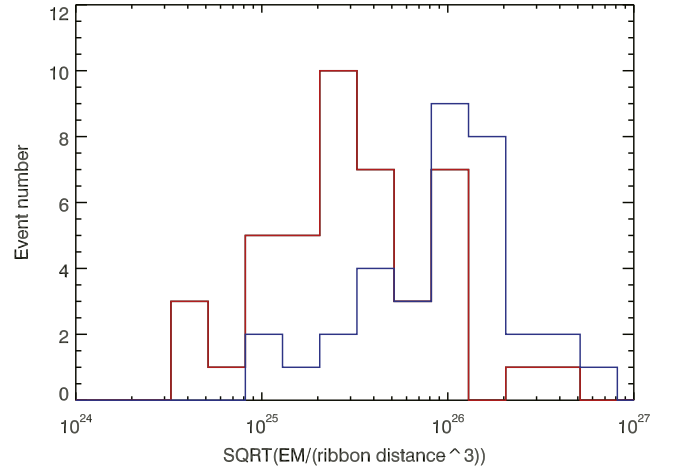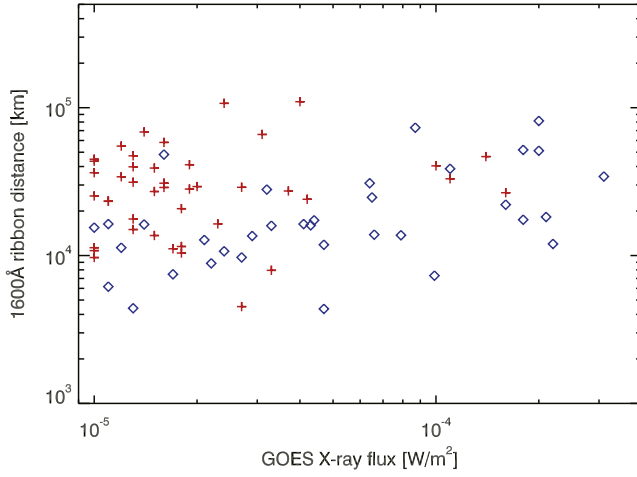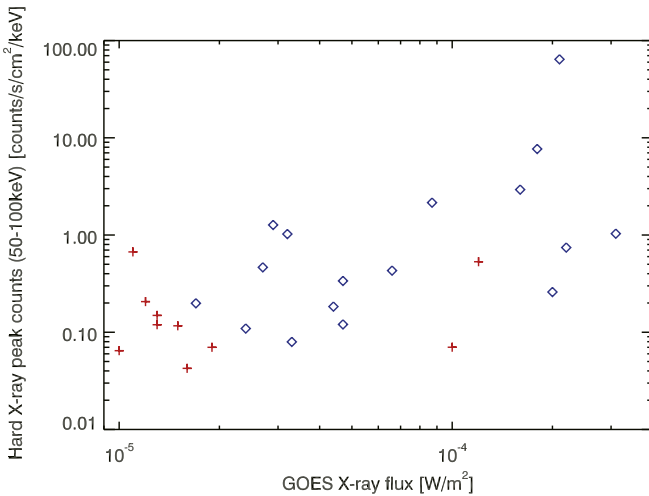
Figure 4. Left: relationship between *GOES* soft X-ray peak flux and flare ribbon distance as estimated from *SDO*/AIA 1600 Å images (taken around derivative peak time of *GOES* soft X-ray data). The diamond (blue) and cross (red) symbols correspond to WLF and NWL events, respectively. Right: histogram of event number for flare density.
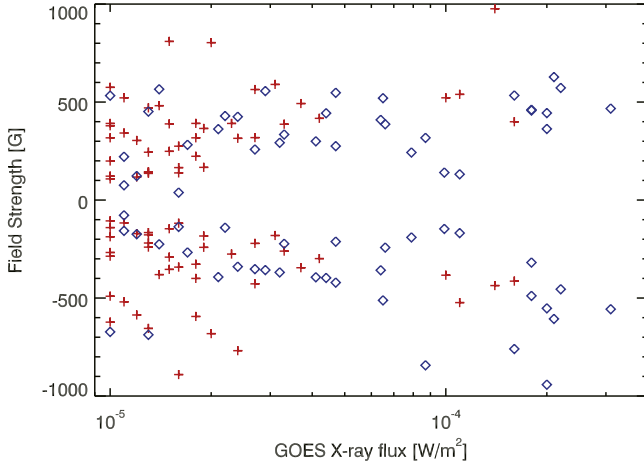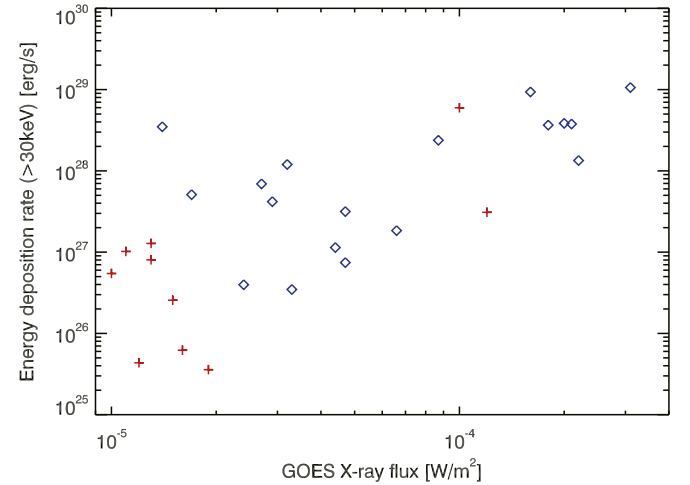

Figure 5. Relationship between *GOES* soft X-ray peak flux and field strength under the 1600 Å flare ribbons, as estimated from *SDO*/HMI data (taken around derivative peak time of *GOES* soft X-ray data). The diamond (blue) and cross (red) symbols correspond to WLF and NWL events, respectively.
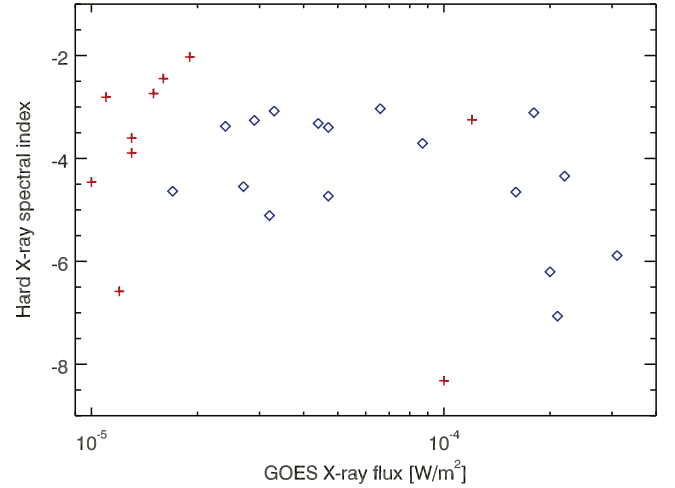
Figure 7. Relationship between *GOES* soft X-ray peak flux and spectral index of hard X-ray, as estimated from *RHESSI* data. The diamond (blue) and cross (red) symbols correspond to WLF and NWL events, respectively.

Figure 6. Relationship between *GOES* soft X-ray peak flux and 50–100 keV hard X-ray peak count obtained from *RHESSI* data. The diamond (blue) and cross (red) symbols correspond to WLF and NWL events, respectively.

Figure 8. Relationship between *GOES* soft X-ray peak flux and energy deposition rate of >30 keV emission, as estimated from *RHESSI* data. The diamond (blue) and cross (red) symbols correspond to WLF and NWL events, respectively.
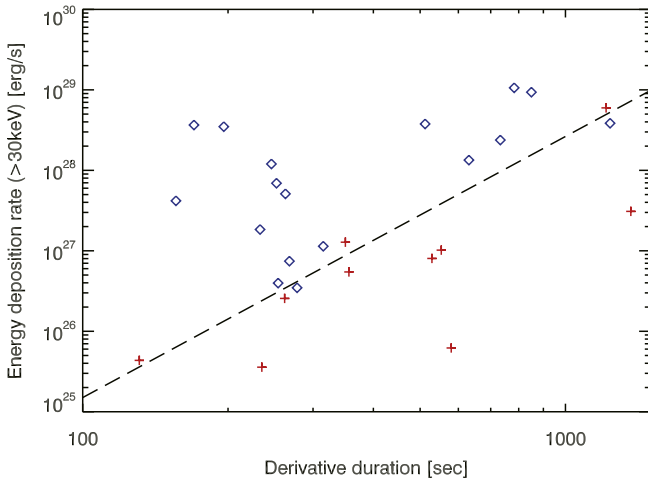
Figure 9. Relationship between the derivative duration estimated from *GOES* X-ray data and energy deposition rate of >30 keV emission, as estimated from *RHESSI* data. The diamond (blue) and cross (red) symbols correspond to WLF and NWL events, respectively. A dashed line separating the two populations which would help to "guide the eye."

found in Figure 8. There is one NWL event in Figure 8 with very high-energy deposition. That is the X1.0-class flare on 2014 October 25, which is due to the very soft power index for this event. The average deposition rate of non-thermal energy was found to be $(2.34 \pm 3.05) \times 10^{28}$ erg s^{-1} for WLF events and $(6.68 \pm 1.77) \times 10^{27}$ erg s^{-1} for NWL events. The deposition rate of WLF events is significantly larger than that of NWL events and this is because the *GOES* soft X-ray flux for WLF events is larger than that for NWL events.

The *X*-axis from the *GOES* soft X-ray flux is then plotted as the derivative duration, and the results are shown in Figure 9. In Figure 9, WLF events are located on the upper left-hand side of the dashed line and NWL evens are located on the lower right-hand side of the dashed line. It is important to note that these data occupy separate regimes in Figure 9. This result suggests that the injection rate of non-thermal electrons is one of the causative factors of WL enhancement.

4. Discussion

The results described in the previous sections can be summarized as follows.

(1) The derivative duration of *GOES* soft X-rays during WLF events is relatively short.

(2) WLF events are characterized by stronger magnetic fields at the energy-release site compared with NWL events from the relationship between the temperature and emission measure.

(3) The separation between two ribbons is shorter for WLF events.

(4) No significant difference exists in field strength under the flare ribbons.

(5) The hard X-ray photon count in the energy range of 50–100 keV and the deposition rate of non-thermal energy (>30 keV) are correlated with the *GOES* soft X-ray flux.

(6) No significant difference exists between the power-law indices of hard X-ray spectra for WLF and NWL events.

(7) WLF events are characterized by larger deposition rates of non-thermal energy compared with NWL events. WLF

events are characterized by a shorter derivative duration for a given deposition rate.

From results (1) and (3), WLF events appear to be small in terms of spatial extent and have a relatively short duration. WLF events are therefore short-lived and exhibit a rapid enhancement phase, whereas NWL events show a gradual enhancement phase. The short separation of flare ribbons implies that the magnetic field structure related to WLF events is compact. During the evolution of a flare, the separation between flare ribbons increases as a function of time, which is consistent with the short duration. Result (3) suggests that the magnetic loop related to WLF events occurs at low altitudes. In general, the magnetic field is stronger at low altitudes than at high altitudes. The energy release of WLF events therefore appears to occur in the lower corona wherein the magnetic field is relatively strong.

Result (2) suggests the existence of strong magnetic fields at the energy-release site for WLF events. The scatter plot of the emission measure and electron temperature reported in Figure 2 of Shibata & Yokoyama (2002) shows four theoretical curves for coronal magnetic field strengths of 5, 15, 50, and 150 G at the energy-release site of the flare. The scatter plot of emission measure and electron temperature reported in this investigation (Figure 2) shows that WLF events are distributed toward the right-hand side of plot, whereas NWL events are located on the left-hand side of the plot. The difference in the distribution of these data may be due to differences in coronal magnetic field strength at the energy-release site. The magnetic field is weaker for NWL events than for WLF events. This finding is consistent with result (3) as the magnetic field is stronger at lower altitudes in the corona.

An attempt was made to check the field strength of the photosphere. However, due to lack of field strength data at the energy-release site, an alternative analysis was undertaken, as described in Section 3.4. No significant difference was observed in the field strength under the flare ribbons.

Results (5) to (7) relate to the hard X-ray observations. As described in Section 1, WL enhancement is correlated with hard X-ray sources in time, location, and energy. Contrary to the expectations of this study, no significant difference was observed in the power-law indices of WLF and NWL events. It therefore follows that the energy distribution of accelerated electrons is similar in both WLF and NWL events. Only very high-energy ($\gg$100 keV) electrons can reach the photosphere (Aboudarham & Henoux 1986; Neidig 1989). Results presented in this work do not show that the fraction of electrons with such high energies is larger in WLF events compared with NWL events. This result does not support the model whereby electrons penetrate directly into the photosphere and emit WL. However, as the conclusions presented here are the result of a statistical analysis, it is possible that some WLF events may result from this process.

The results presented in this investigation indicate that to enhance WL emissions, a large number of accelerated electrons must precipitate within a short period, thereby leading to very rapid heating of the atmosphere. Result (7) suggests that rapid heating is important and that a threshold exists in terms of the injection rate of non-thermal electrons required to generate WL emission.

Through this statistical study, it has been shown that WLF events are characterized by stronger magnetic fields at the energy-release site compared with NWL events. This strong

magnetic field may be a factor in the enhancement of WL emission. It is important to consider how a strong magnetic field may be related to WLF events. Two models explain WL emission and indicate that the energy-release region is characterized by a strong magnetic field. In the solar flare model based on magnetic reconnection, the energy-release rate increases if the energy-release region has a strong magnetic field and electrons are accelerated. Hard X-ray sources appear at the region wherein the magnetic field is strongest along the flare ribbon (Asai et al. 2002). Large numbers of electrons are accelerated and this leads to the enhancement of WL emission. The strong magnetic field may also be considered in terms of the trapping efficiency of accelerated electrons in the flare loop. If the top part of the loop is characterized by a stronger magnetic field than that of the foot-point region, the magnetic mirror ratio between the top and the foot-point becomes small and the loss-cone angle is large. Because of this effect, a larger number of accelerated electrons can precipitate into the foot-point region within a short period of time. The trapping efficiency of the loop is therefore lower and most of the accelerated electrons precipitate directly into the foot-point region. This scenario is consistent with results obtained in this study.

Investigating the magnetic structure of a flare region could prove interesting and may reveal how and why the magnetic field strength at the energy-release site is related to the generation mechanism of WLF events.

5. Conclusion

A statistical study has been presented comprising 101 solar flares observed using the visible continuum filter of *Hinode*/SOT and *SDO*/HMI for *GOES* M- and X-class flares occurring during the period from 2011 January to 2016 February. Of these 101 events, 49 WLF events and 52 NWL events were identified on the basis of the existence of an enhancement of the visible continuum images obtained using *Hinode*/SOT and *SDO*/HMI. The WLF events are characterized by short duration, a high temperature in the *GOES* soft X-ray data, and short distance between two flare ribbons in the *SDO*/AIA 1600 Å observations. No significant difference was observed between WLF and NWL events in terms of power-law indices, flux of non-thermal photons (50–100 keV), or in the deposition rate of the non-thermal energy. However, a clear relationship between the injection rate of non-thermal energy and derivative duration was observed. These results indicate that during WLF events, accelerated electrons precipitate in a short time period, thereby leading to rapid heating of the atmosphere. The similarity in the power-law index of hard X-ray spectra, as well as the similar deposition rate of non-thermal energy, does not indicate that the fraction of electrons with very high energies ($\gg$100 keV) is larger in WLF events compared with NWL events. Relatively low-energy ($<$100 keV) electrons appear to contribute to the enhancement of WL. This finding is consistent with studies detailing the energy budget between non-thermal electrons and WL emission (Watanabe et al. 2010).

The statistical analysis presented here suggests that the non-thermal energy deposition rate and the magnetic field strength at the energy-release site are significant in WL emission in solar flares. In future work, investigating the magnetic field structure around the energy-release site would be interesting to describe more fully the environment of non-thermal

electrons. The physical relationship between the magnetic field structure and the energy of electrons should therefore be the subject of a detailed investigation. Such a study would be expected to provide insight into not only the process of WL emission but also into the acceleration of electrons in solar flares.

It is useful to derive the color temperature of WLF when its energy source is studied (Watanabe et al. 2013; Kerr & Fletcher 2014). However, we did not derive it in this paper because we focused on the difference of WLF and NWL events. In the future, we would like to perform this kind of detailed WLF analyses that would provide unique constraints for radiative-hydrodynamic flare models and might reveal lower atmospheric heating differences in impulsive flares and non-impulsive flares. Moreover, Kowalski et al. (2013) showed how the NUV and optical continuum spectral properties of M dwarf flares vary from impulsive flare events to gradual flare events, where the type of flare (impulsive versus gradual) is determined from a similar quantity as the "impulsivity." It would also be interesting to discuss how their results for M dwarf WLFs connect with our study.

References

Aboudarham, J., & Henoux, J. C. 1986, A&A, 156, 73
Asai, A., Masuda, S., Yokoyama, T., et al. 2002, ApJL, 578, L91
Battaglia, M., & Kontar, E. P. 2011, A&A, 533, L2
Battaglia, M., & Kontar, E. P. 2012, ApJ, 760, 142
Brown, J. C. 1971, SoPh, 18, 489
Carrington, R. C. 1859, MNRAS, 20, 13
Ding, M. D., Liu, Y., Yeh, C.-T., & Li, J. P. 2003, A&A, 403, 1151
Fletcher, L., Hannah, I. G., Hudson, H. S., & Metcalf, T. R. 2007, ApJ, 656, 1187
Golub, L., DeLuca, E., Austin, G., et al. 2007, SoPh, 243, 63
Hudson, H. S., Wolfson, C. J., & Metcalf, T. R. 2006, SoPh, 234, 79
Ichimoto, K., Lites, B., Elmore, D., et al. 2008, SoPh, 249, 233
Isobe, H., Kubo, M., Minoshima, T., et al. 2007, PASJ, 59, S807
Jess, D. B., Mathioudakis, M., Crockett, P. J., & Keenan, F. P. 2008, ApJL, 688, L119
Kano, R., Sakao, T., Hara, H., et al. 2008, SoPh, 249, 263
Kerr, G. S., & Fletcher, L. 2014, ApJ, 783, 98
Kowalski, A. F., Hawley, S. L., Wisniewski, J. P., et al. 2013, ApJS, 207, 15
Krucker, S., Hudson, H. S., Jeffrey, N. L. S., et al. 2011, ApJ, 739, 96
Krucker, S., Saint-Hilaire, P., Hudson, H. S., et al. 2015, ApJ, 802, 19
Kuhar, M., Krucker, S., Martínez Oliveros, J.-C., Battaglia, M., & Kleint, L. 2016, ApJ, 816, 6
Lemen, J. R., Title, A. M., Akin, D. J., et al. 2012, SoPh, 275, 17
Lin, R. P., Dennis, B. R., Hurford, G. J., et al. 2002, SoPh, 210, 3
Machado, M. E., Avrett, E. H., Falciani, R., et al. 1986, in The Lower Atmosphere of Solar Flares, ed. D. F. Neidig (Sunspot: NSO), 483
Machado, M. E., Emslie, A. G., & Avrett, E. H. 1989, SoPh, 124, 303
Martínez Oliveros, J.-C., Hudson, H. S., Hurford, G. J., et al. 2012, ApJL, 753, L26
Matthews, S. A., van Driel-Gesztelyi, L., Hudson, H. S., & Nitta, N. V. 2003, A&A, 409, 1107
Metcalf, T. R., Alexander, D., Hudson, H. S., & Longcope, D. W. 2003, ApJ, 595, 483
Metcalf, T. R., Canfield, R. C., & Saba, J. L. R. 1990, ApJ, 365, 391
Namekata, K., Sakaue, T., Watanabe, K., et al. 2017, PASJ, 69, 7

Neidig, D. F. 1989, SoPh, 121, 261
Neupert, W. 1968, ApJL, 153, L59
Pesnell, W. D., Thompson, B. J., & Chamberlin, P. C. 2012, SoPh, 275, 3
Scherrer, P. H., Schou, J., Bush, R. I., et al. 2012, SoPh, 275, 207
Schou, J., Scherrer, P. H., Bush, R. I., et al. 2012, SoPh, 275, 229
Shibata, K., & Yokoyama, T. 1999, ApJL, 526, L49
Shibata, K., & Yokoyama, T. 2002, ApJ, 577, 422

Shimizu, T., Nagata, S., Tsuneta, S., et al. 2008, SoPh, 249, 221
Suematsu, Y., Tsuneta, S., Ichimoto, K., et al. 2008, SoPh, 249, 197
Tsuneta, S., Suematsu, Y., Ichimoto, K., et al. 2008, SoPh, 249, 167
Wang, H.-M. 2009, RAA, 9, 127
Watanabe, K., Krucker, S., Hudson, H., et al. 2010, ApJ, 715, 651
Watanabe, K., Masuda, S., & Segawa, T. 2012, SoPh, 279, 317
Watanabe, K., Shimizu, T., Masuda, S., et al. 2013, ApJ, 776, 123